Experiments on Shock Induced Laminar-Turbulent Transition on a Flat Plate at Mach 6

Sebastian Willems⋆ and Ali Gülhan⋆
⋆German Aerospace Center (DLR), Institute of Aerodynamics and Flow Technology,
Supersonic and Hypersonic Technology Department, Linder Höhe, 51147 Köln, Germany

Abstract

This paper presents the results of the experiments performed in the hypersonic wind tunnel H2K in the framework of the ESA technology research project "Laminar to Turbulent Transition in Hypersonic Flows". The investigations include the free boundary layer transition on a flat plate as well as the influence of a shock wave boundary layer interaction on the transition. The experiments were performed at Mach 6.0 at three different unit Reynolds numbers and with a translational displacement of the shock generator. Besides the optical methods schlieren photography and infrared thermography several high-speed intrusive sensors were used. Heat flux measurements were carried out using coaxial thermocouples, thin film gauges and an atomic layer thermo pile. Kulite and PCB sensors were used for pressure measurements. This paper concentrates on the heat flux measurements and includes just a glance on the pressure measurements.

Symbols

α	angle of the shock generator to the base plate
μ	dynamic viscosity
ω	exponent of the power-law viscosity law
c_f	skin friction coefficient
F_c	transfer function for compressible flow
p	static pressure
Pr	Prandtl number
r	recovery factor
Re_u	unit Reynolds number
Re_x	Reynolds number based on X-coordinate
Re_{af}	Reynolds analogy factor
St	Stanton number
T	static temperature
x	X-coordinate with 0 mm $\hat{=}$ leading edge
x_{shock}	X-coordinate of the theoretic shock impingement
y	Y-coordinate with 0 mm $\hat{=}$ symmetry plane

Superscripts / Subscripts

0	reservoir conditions
$*$	reference conditions
∞	free-stream flow conditions
e	flow conditions at boundary layer edge
lam	laminar boundary layer
$turb$	turbulent boundary layer
w	wall conditions

1. Introduction

The transition from a laminar to a turbulent boundary layer is attended by an increase of the heat flux and drag. Therefore the correct prediction of this process is essential for the design of future hypersonic vehicles and their thermal protection systems. A great influence onto the transition process has the shock wave boundary layer interaction (SWBLI). In order to study these phenomena in the framework of the ESA-TRP "Laminar to turbulent transition in hypersonic flows" experiments in three different facilities using several measuring techniques have been carried out. This paper describes the results of the experiments performed in the hypersonic wind tunnel H2K at the German Aerospace Center (DLR) in Cologne.

The transition region could be visualized by means of the quantitive infrared thermography and using a PEEK insert with low thermal conductivity. Additional flow visualization was carried out by Schlieren pictures that shows the positions of all relevant shock waves. Kulite and PCB sensors measured the static and dynamic pressure distributions along the base plate. For the first time thin film gauges, coaxial thermocouples and an atomic layer thermo pile (ALTP) were used for heat flux measurements in H2K. It has been noticed that the poor signal to noise ratio of the thin film gauges and the coaxial thermocouples does not allow to measure the dynamics of the heat flux. In contrary ALTP sensors provided useful static and dynamic data. The formation growth an destruction of second (Mack) modes was measured with ALTP and PCB sensors. Kulite sensors measured the pressure fluctuations at low frequencies arising from the SWBLI.

2. Experimental setup

2.1 Wind tunnel

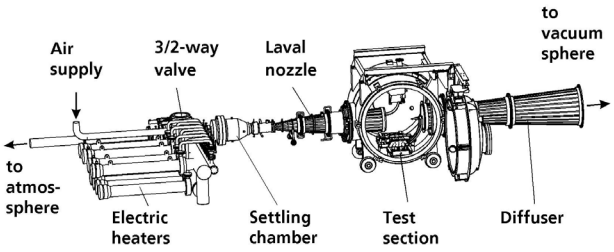

(a) Sketch of H2K

Flow conditions			Model configurations		
$Re_{u,\infty}$ $\left[\frac{10^6}{m}\right]$	T_0 [K]	p_0 [MPa]	w/o shock	4° @ 239 mm	4° @ 331 mm
12	500	1.50	IR, P, T	IR, P, T	IR, P, T
6	500	0.74	IR, P, T	IR, P, T	IR, P, T
3	600	0.50	IR, P, T	IR, P, T	IR, P, T

(b) Test matrix for the H2K

Figure 1: The hypersonic wind tunnel Cologne (H2K)

The experiments were performed in the hypersonic wind tunnel Cologne (H2K) [6]. It is a blow-down wind tunnel with a free jet test section and a test time of 30 s (figure 1a). For the experiments a Mach 6 contoured nozzle with an exit diameter of 600 mm was used. The test gas air is heated with resistance heaters. Figure 2b shows the test section with the model.

2.2 Model

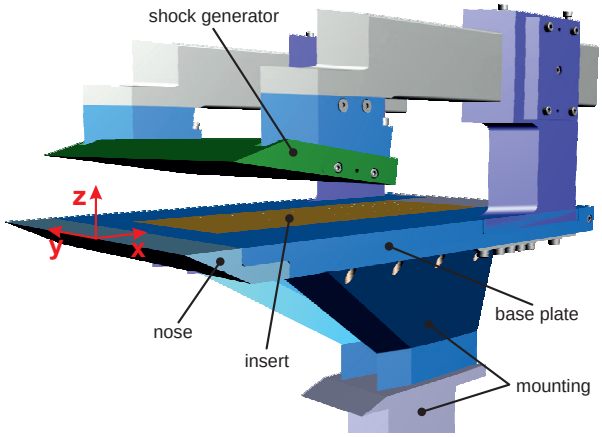

(a) CAD model with definition of the coordinate system

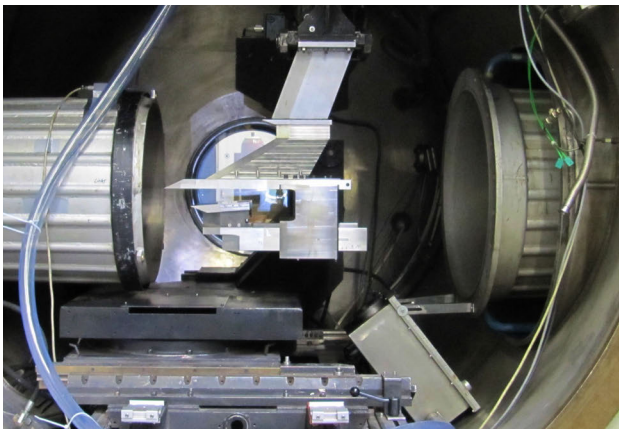

(b) model inside the test section of the H2K

Figure 2: Experimental set-up

As shown in figure 2a the model consists of the following main parts:

- A flat base plate 600 mm in length and 340 mm in width, with an exchangeable nose with a sharp leading edge and a ramp of 25° towards the underside.

- Different measuring inserts embedded into the base plate, 400 mm in length and 150 mm in width
- A wedge as a shock generator, 190 mm in length and 340 mm in width. It has a leading edge with a radius of 0.1 mm and a ramp to the upside of of 25°. The shock generator is moveable in flow direction and can be installed at different angles of attack. All H2K experiments with the shock generator were performed with an angle of attack of the shock generator of $\alpha = 4°$.
- The mounting system

The midpoint of the leading edge of the base plate's nose is the origin of the coordinate system used in this paper. The x-axis points in the flow direction, the y-axis is parallel to the leading edge and the z-axis is the normal vector of the base plate pointing towards the shock generator. The defined coordinate system is also shown in figure 2a. With respect to the standard H2K support arm, the model was mounted upside down in the test section (figure 2b).

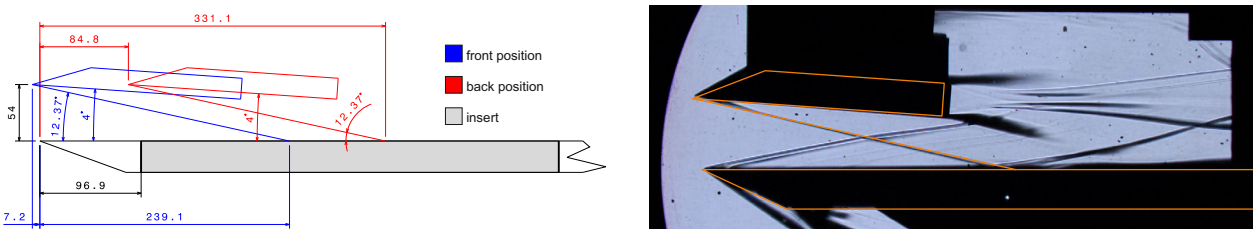

(a) Theoretic shock generator positions

(b) Comparison of theoretical and real shock impingement positions

Figure 3: Shock generator and shock impingement positions

Both positions of the shock generator used for the experiments in H2K are shown in figure 3. In reality the generated shock is a little bit upstream of the estimated position based on the equations provided by NACA [1]. Derived from figure 3b the extrapolated shock impingement with the shock generator at the front postion is about 9 mm upstream the estimated position and for the back position derived it is about 17 mm upstream the estimated position. As these differences have no effect whether a sensor is upstream or downstream the impingement and the real locations are not very precise, the labels of the configurations inside this paper base on the theoretic values.

2.3 Instrumentation

Three different measuring inserts were used for the experiments in H2K. One insert made of PEEK was used for the infrared thermography. Two inserts made of steel are equipped with different sensors as shown in figures 4a and 4b.

1. Insert "IR"
   - It is purely made of PEEK and used for heat flux measurements by means of infrared thermography.
2. Insert "T" with a sensor configuration as shown in figure 4a
   - 16 thin film gauges sampled at 5 MHz
   - 24 coaxial thermocouples type E sampled at 100 Hz
   - 14 Kulite pressure sensors sampled at 100 kHz
3. Insert "P" with a sensor configuration as shown in figure 4b
   - 5 coaxial thermocouples type E sampled at 5 MHz
   - 1 ALTP sampled at 5 MHz
   - 5 PCB pressure sensors (a 6^{th} sensor was mounted blind and used as reference) sampled at 5 MHz

2.4 Test Matrix

Each combination of the three shock generator positions (without, front position and back position) and the three measuring inserts was tested at three different unit Reynolds numbers (3, 6 and $12 \cdot 10^6 \frac{1}{\mathrm{m}}$). The complete test matrix is given in figure 1b.

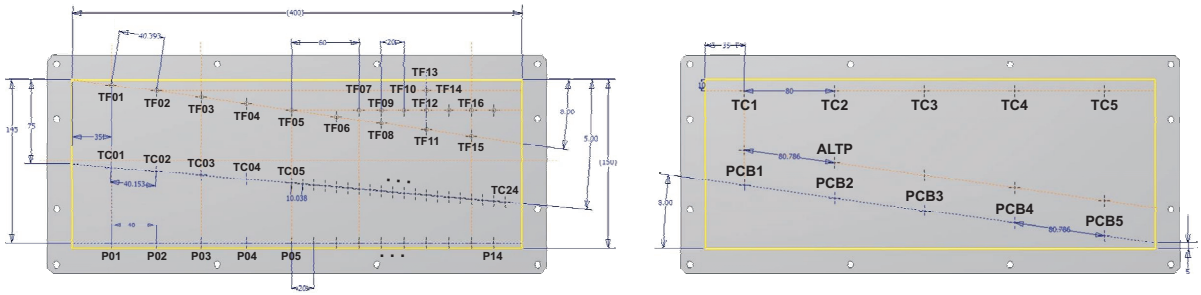

(a) Sensor positions for insert “T”

(b) Sensor positions for insert “P”

Figure 4: Positions and numbering of the sensors

3. Measurement Techniques and Procedures

3.1 Data acquisition

The surface temperature on the PEEK insert was measured with a FLIR SC3000 infrared camera [5]. The PCB sensors in insert “P” are connected to signal conditioner modules PCB 482C05 and their output signals are measured with Adlink PXI-9816D/512 digitizers, which enable a 16 bit resolution and a sample rate of 5 MHz. The ALTP sensor in insert “P” is connected to a cosytec FVST5 amplifier and the outputs are also measured with the Adlink digitizers. The coaxial thermocouples of insert “P” are amplified using Rohrer Hero NG9303C amplifiers and connected to the Adlink digitizers. The Kulite sensors in the insert “T” are connected to National Instruments PXIe-4331 bridge modules, which enable a 24 bit resolution and a sample rate of 100 kHz. The thin film gauges in the insert “T” are amplified with the Dewetron DAQP-STG amplifiers and their output signals are transformed with the Adlink digitizers. The coaxial thermocouples of the insert “T” are again amplified with the Rohrer amplifiers but their outputs are connected to the low speed measuring unit of H2K and sampled at 100 Hz.

The calibration data of the PCB and thin film gauges is based on the manufacturer’s calibration. For the coaxial thermocouples and the ALTP sensor the standard values of the sensitivity are used. In addition the offset of the ALTP sensor is recalculated by the measurements before the wind tunnel start. The Kulite sensors are calibrated using the Baratron reference pressure sensor of the H2K.

3.2 Data processing

3.2.1 Stanton number from infrared pictures

The raw data of the infrared camera are transferred to heat fluxes and Stanton numbers using the in-house tool Visual-HeatFlow (for the algorithm see [2]). The recovery factor for the post-processing of the infrared images is always set to the value of a laminar boundary layer $r_{lam} = \sqrt{Pr}$. The correction of the image distortion are performed using the algorithm of Tsai [8].

The theoretical Stanton number curves for laminar and turbulent boundary layers use the free stream conditions computed from measured values of the reservoir conditions and measured wall temperatures. The equation used for a laminar boundary is given by Korkegi [4].

$$c_{f,lam} = \frac{0.664}{\sqrt{Re_x}} \left(\frac{T^*}{T_\infty} \right)^{\frac{\omega-1}{2}} \tag{1}$$

$$T^* = T_\infty \left[0.42 + 0.58 \frac{T_w}{T_\infty} + 0.032 M_\infty^2 \right] \tag{2}$$

It is derived from the reference temperature method using the power-law viscosity law. As the Sutherland’s law is known to be more accurate for low temperatures, its use for the ratio of the viscosities at reference and at free stream temperature should improve the results.

$$c_{f,lam} = \frac{0.664}{\sqrt{Re_x}} \sqrt[4]{\frac{T^*}{T_\infty}} \sqrt{\frac{T_\infty + 110.4\,\mathrm{K}}{T^* + 110.4\,\mathrm{K}}} \tag{3}$$

The comparison in figure 9b shows significant differences between the two viscosity laws. For $Re_{\mathrm{u},\infty} = 3 \cdot 10^6 \, \frac{1}{\mathrm{m}}$ the measured values are between these theoretical curves, but the gradient is not the same. As Sutherland's law should be more accurate at low temperatures and it is closer to the values of $Re_{\mathrm{u},\infty} = 6 \cdot 10^6 \, \frac{1}{\mathrm{m}}$ it is used for the theoretical Stanton number values of a laminar boundary layer within this report.

In case of a turbulent boundary layer not only the viscosity law but also the basic equation is ambiguous. The equation given by Korkegi [4] is based on the equation of Blasius and uses the power-law viscosity law. Below it is written with the additional recovery factor r_{turb}:

$$c_{f,turb} = \frac{0.0592}{\sqrt[5]{Re_x}} \left(\frac{T^*}{T_\infty} \right)^{\frac{\omega-4}{5}} \tag{4}$$

$$T^* = T_\infty \left[0.55 + 0.45 \frac{T_w}{T_\infty} + 0.035 r_{turb} M_\infty^2 \right] \tag{5}$$

The use of Sutherland's law of viscosity for the Korkegi equation leads to:

$$c_{f,turb} = \frac{0.0592}{\sqrt[5]{Re_x}} \sqrt{\frac{T_\infty}{T^*}} \sqrt[5]{\frac{T_\infty + 110.4\,\mathrm{K}}{T^* + 110.4\,\mathrm{K}}} \tag{6}$$

The solutions of the implicit equation of van Driest [9] are always at higher values.

$$\frac{0.242}{\sqrt{c_f F_c}} = 0.41 + \log_{10} \left(Re_x F_x c_f F_c \right) \tag{7}$$

It uses the following transfer functions for compressible flows. They are formulated here according to Hopkins and Inouye [3] including the recovery factor r_{turb}, which is not considered in the original paper of van Driest [9].

$$F_c = \frac{m}{(\arcsin\alpha + \arcsin\beta)^2} \qquad F_\theta = \frac{\mu_e}{\mu_w} \quad F_x = \frac{F_\theta}{F_c} \tag{8}$$

$$\alpha = \frac{m - 1 + F}{\sqrt{(m + 1 + F)^2 - 4F}} \qquad m = r_{turb} \frac{\kappa - 1}{2} M_e^2 \tag{9}$$

$$\beta = \frac{m + 1 - F}{\sqrt{(m + 1 + F)^2 - 4F}} \qquad F = \frac{T_w}{T_e} \tag{10}$$

In the original paper of van Driest [9] the power-law viscosity law for F_θ is used.

$$F_{\theta,\mathrm{power-law}} = \left(\frac{T_e}{T_w} \right)^\omega \tag{11}$$

But it is also possible to use Sutherland's law for F_θ.

$$F_{\theta,\mathrm{Sutherland}} = \left(\frac{T_e}{T_w} \right)^{\frac{3}{2}} \frac{T_w + 110.4\,\mathrm{K}}{T_e + 110.4\,\mathrm{K}} \tag{12}$$

White [10] formulated another equation computing even higher values than the van Driest equation.

$$c_{f,turb} = \frac{0.455}{F_c} \cdot \left[\ln \left(\frac{0.06 Re_x F_\Theta}{\sqrt{F_c F}} \right) \right]^{-2} \tag{13}$$

Also challenging is the choice of the parameters especially the Reynolds analogy factor Re_{af} for the transformation of the skin-friction coefficient to the Stanton number.

$$St = \frac{Re_{af} c_f}{2} \tag{14}$$

The values of the parameters for the calculation of the theoretical curves are set in analogy to Schülein and Wagner [7] as $\omega = 0.76$, $Pr = 0.72$, $r_{turb} = 0.89$ and $Re_{af} = Pr^{-2/3}$.

A comparison of the results of the different equations is given in figure 9b. The theoretical Stanton number curves of a turbulent boundary layer split into four groups. The lowest values are from the equation of Korkegi using the power-law viscosity law. The second group consists of the equation of Korkegi using Sutherland's law and the equation of van Driest using the power-law viscosity law. The second group consists of the van Driest equation using Sutherland's law and White's equation using the power-law. The highest values gives White's equation with the Sutherland's law. As the last one is the closest to the measured values with $Re_{u,\infty} = 12 \cdot 10^6 \frac{1}{m}$ and $Re_{u,\infty} = 16 \cdot 10^6 \frac{1}{m}$ and the explicit formulation simplifies the processing the White's equation using Sutherland's law is used for the theoretical Stanton number values of a turbulent boundary layer within this report.

3.2.2 Frequency spectra and spectrograms

The averaged frequency spectra, shown in section 4.4, are based on twenty-five-million data points at stable flow conditions (5 s @ 5 MHz). They are divided into 1000 blocks with 50 000 samples each overlapping each other by 50%. All values are normalized and then each block is multiplied with the Hann function. For each block the power spectral density is computed. The arithmetic mean of all spectra is the final result. Hence the frequency spectra show root mean square values scaled with the frequency.

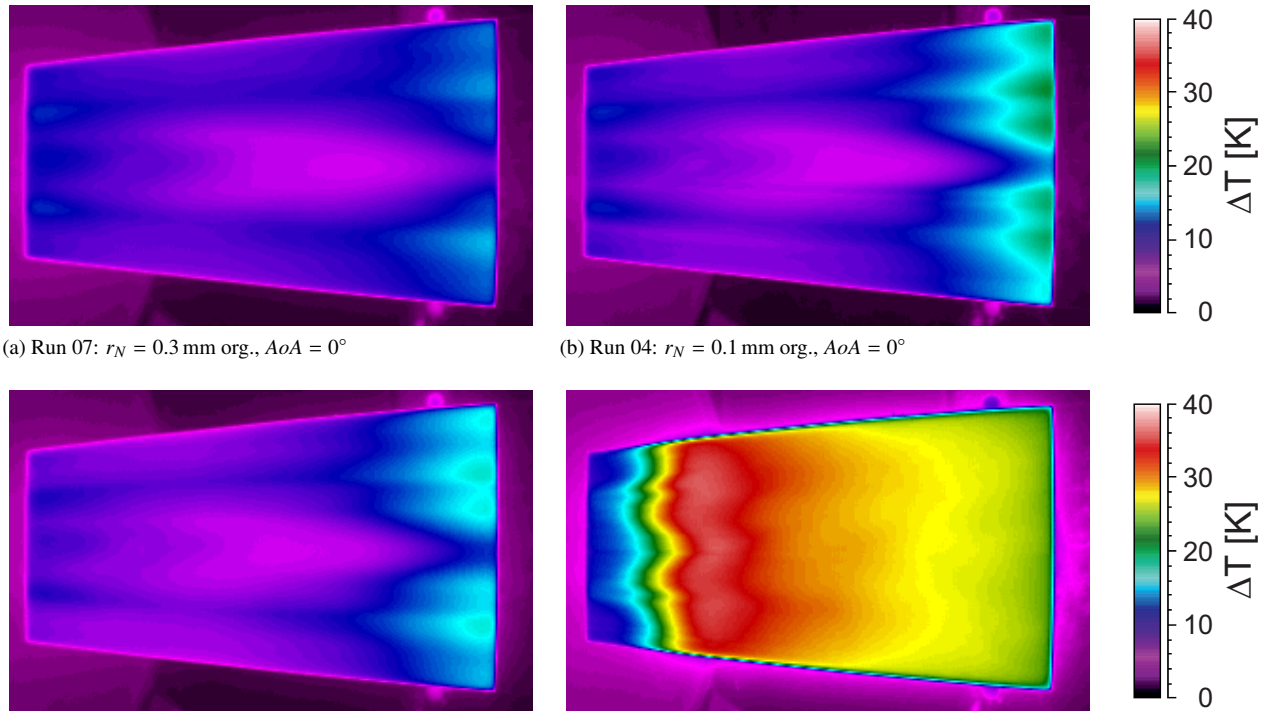

(a) Run 07: $r_N = 0.3$ mm org., $AoA = 0°$

(b) Run 04: $r_N = 0.1$ mm org., $AoA = 0°$

(c) Run 17: $r_N = 0.1$ mm new, $AoA = 0°$

(d) Run 18: $r_N = 0.0$ mm new, $AoA = 0°$

Figure 5: Temperature increase on the PEEK insert due to free transition for various nose radii and angles of attack at $Re_{u,\infty} = 16 \cdot 10^6 \frac{1}{m}$

4. Results and discussion

4.1 Influence of the nose radius

The first runs in H2K with the leading edges of the test model used in HEG revealed that they are not suitable for the experiments in H2K. Neither with a nose radius r_N of 0.3 mm (figure 5a) nor 0.1 mm (figure 5b) the transition was completed on the measuring insert. Even with the maximum unit Reynolds number of $Re_{u,\infty} = 18.5 \cdot 10^6 \frac{1}{m}$ the transition was not completed at a path length of 497 mm, which is the position of the insert's trailing edge (figure 6a). In addition the infrared pictures reveal that the transition region is very frayed. A revised version of the nose with a

radius of 0.1 mm (figure 5c) is a little less frayed, but not substantially different. Therefore the nose was sharpened by hand as for the experiments in RWG. This method leads to a transition far upstream (figure 5d) and even a completed transition on the measuring insert for a unit Reynolds number of $Re_{u,\infty} = 6 \cdot 10^6 \frac{1}{m}$ (figure 8b).

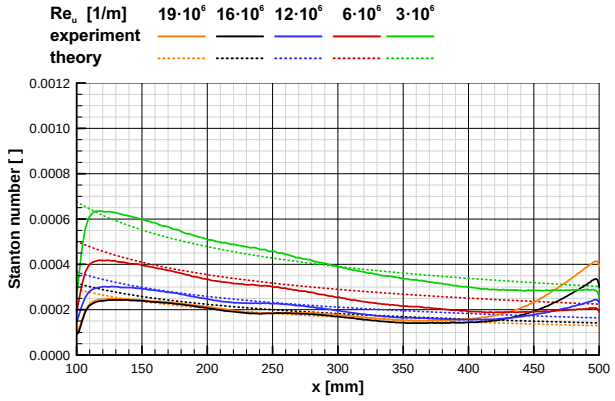

(a) Distribution of the Stanton number with $r_N = 0.1$ mm and various Reynolds numbers

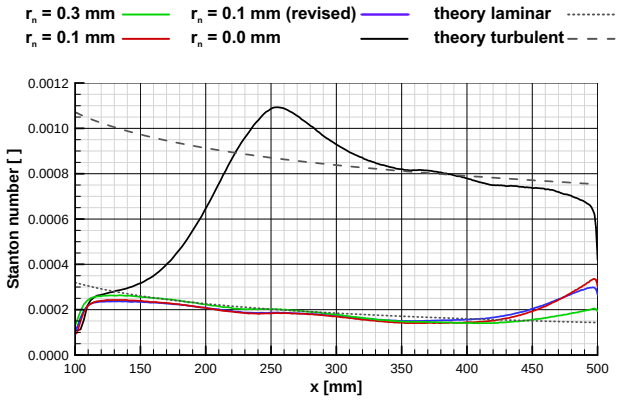

(b) Distribution of the Stanton number with $Re_{u,\infty} = 16 \cdot 10^6 \frac{1}{m}$ and various nose radii

Figure 6: Distribution of the Stanton number in the symmetry plane at $Ma = 6.0$ and $AoA = 0°$ for various Reynolds numbers and nose radii

4.2 Schlieren and infrared pictures

Although the Schlieren pictures in H2K, which are optimized for long duration testing, do not show the turbulent structures they reveal some basic information of the flow field for the interpretation of the results. Figure 7 compares the Schlieren pictures of low Reynolds number runs ($Re_{u,\infty} = 3 \cdot 10^6 \frac{1}{m}$) and high Reynolds number runs ($Re_{u,\infty} = 12 \cdot 10^6 \frac{1}{m}$) as well as different shock generator positions. The shadow of the sharp leading edge shock is stronger at the high Reynolds number condition (figure 7c) compared to the low Reynolds number run (figure 7a), because the absolute pressure increase is higher. When the shock generator is at the back position ($x_{shock} = 331$ mm) the shock from the leading edge is reflected by the shock generator (figures 7g and 7i). The reflected shock hits the base plate again downstream of the major impingement. When the shock generator is at the front position ($x_{shock} = 239$ mm) the shock from the leading edge misses the shock generator and is not reflected (figures 7d and 7f). The Schlieren pictures of the low Reynolds number runs with shock generator show a shock wave whose origin is upstream the shock impingement point and which does not appear in the high Reynolds number runs. The reason for this is a separation bubble that forms due to the SWBLI at low Reynolds numbers.

The infrared pictures of the PEEK insert (figure 8) show that the free transition (without shock generator) is not a straight line figures 8a and 8c. This has to be taken into account when interpreting the results of sensor data which don't have the same Y-coordinate. This is true for most of the sensor rows used in this project. The waviness of the transition region increases with a decreasing unit Reynolds number. With the shock generator at the front position at the high Reynolds number condition transition occurs more or less on a straight line (figure 8f). This becomes a little wavy again for the middle Reynolds number. In case of the low Reynolds number, the transition region is streaky and has a bean like shape (figure 8d). Probably the transition process is not completed in this case and the boundary layer relaminerizes. The values in figures 8d and 8f with $x < 140$ mm are not valid, since the view of the camera is blocked by the shock generator there. In analogy to that values with $x < 240$ mm in figures 8g and 8i are invalid. In contrast to the runs with free transition and the shock generator at the front position the highest Reynolds number does not lead to the highest but to the lowest Stanton numbers when the shock generator is at the back position. In figure 8i also the impingement of the reflected shock from the leading edge is visible at $x \approx 400$ mm.

The extraction of the values in the symmetry plane (figures 9 and 10) facilitates quantitative analysis. In figure 9a the Stanton number distributions of free transitions without a shock impingement for various unit Reynolds numbers are plotted. Additionally there are the theoretical curves for laminar (dotted lines) and turbulent boundary layers (dashed lines). Figure 9b is includes the same curves but instead of the X-coordinate the Reynolds number is used for the abscissa. Therefore the theoretical curves are almost congruent.

The measured values of the Stanton number before the transition onset match quite well the theoretical curves of a laminar boundary layer. The measured values of the Stanton number downstream the transition end are higher than the theoretical curves of a turbulent boundary layer. But they seem to converge slowly to these curves. Obviously

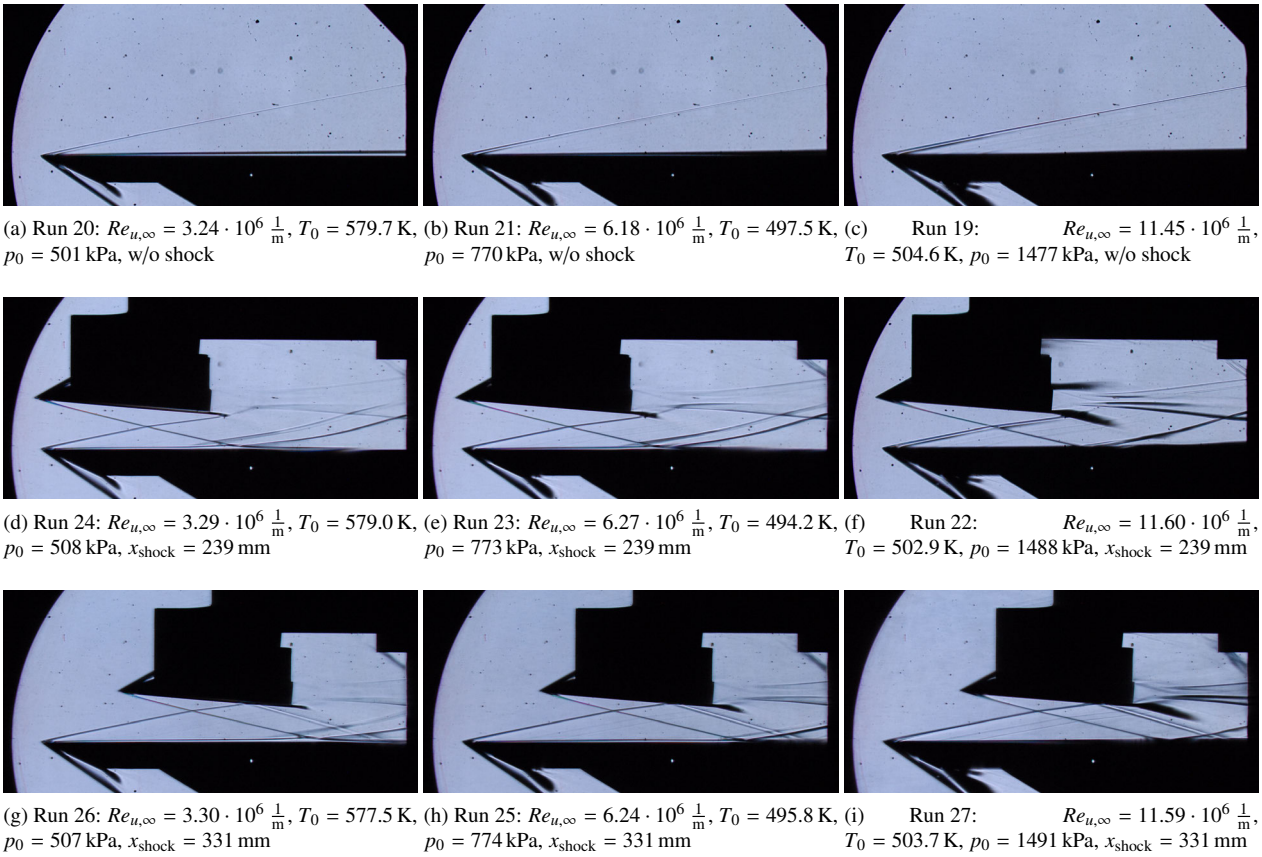

(a) Run 20: $Re_{u,\infty} = 3.24 \cdot 10^6 \frac{1}{\mathrm{m}}$, $T_0 = 579.7\,\mathrm{K}$, $p_0 = 501\,\mathrm{kPa}$, w/o shock

(b) Run 21: $Re_{u,\infty} = 6.18 \cdot 10^6 \frac{1}{\mathrm{m}}$, $T_0 = 497.5\,\mathrm{K}$, $p_0 = 770\,\mathrm{kPa}$, w/o shock

(c) Run 19: $Re_{u,\infty} = 11.45 \cdot 10^6 \frac{1}{\mathrm{m}}$, $T_0 = 504.6\,\mathrm{K}$, $p_0 = 1477\,\mathrm{kPa}$, w/o shock

(d) Run 24: $Re_{u,\infty} = 3.29 \cdot 10^6 \frac{1}{\mathrm{m}}$, $T_0 = 579.0\,\mathrm{K}$, $p_0 = 508\,\mathrm{kPa}$, $x_{\mathrm{shock}} = 239\,\mathrm{mm}$

(e) Run 23: $Re_{u,\infty} = 6.27 \cdot 10^6 \frac{1}{\mathrm{m}}$, $T_0 = 494.2\,\mathrm{K}$, $p_0 = 773\,\mathrm{kPa}$, $x_{\mathrm{shock}} = 239\,\mathrm{mm}$

(f) Run 22: $Re_{u,\infty} = 11.60 \cdot 10^6 \frac{1}{\mathrm{m}}$, $T_0 = 502.9\,\mathrm{K}$, $p_0 = 1488\,\mathrm{kPa}$, $x_{\mathrm{shock}} = 239\,\mathrm{mm}$

(g) Run 26: $Re_{u,\infty} = 3.30 \cdot 10^6 \frac{1}{\mathrm{m}}$, $T_0 = 577.5\,\mathrm{K}$, $p_0 = 507\,\mathrm{kPa}$, $x_{\mathrm{shock}} = 331\,\mathrm{mm}$

(h) Run 25: $Re_{u,\infty} = 6.24 \cdot 10^6 \frac{1}{\mathrm{m}}$, $T_0 = 495.8\,\mathrm{K}$, $p_0 = 774\,\mathrm{kPa}$, $x_{\mathrm{shock}} = 331\,\mathrm{mm}$

(i) Run 27: $Re_{u,\infty} = 11.59 \cdot 10^6 \frac{1}{\mathrm{m}}$, $T_0 = 503.7\,\mathrm{K}$, $p_0 = 1491\,\mathrm{kPa}$, $x_{\mathrm{shock}} = 331\,\mathrm{mm}$

Figure 7: Schlieren pictures for high and low unit Reynolds number and various shock positions

the transition for the lowest unit Reynolds number is not completed on the insert. For the highest Reynolds number the transition probably begins upstream the insert. Interesting is the fact, that the overshoot of the Stanton number for $Re_{\mathrm{u},\infty} = 16 \cdot 10^6 \frac{1}{\mathrm{m}}$ is much more prominent and the maximum Stanton number is higher than for $Re_{\mathrm{u},\infty} = 12 \cdot 10^6 \frac{1}{\mathrm{m}}$ whereas the latter one is lower than for $Re_{\mathrm{u},\infty} = 6 \cdot 10^6 \frac{1}{\mathrm{m}}$.

Figure 10a includes the Stanton number distributions of free transitions and with the shock generator at both positions versus the X-coordinate. The same curves are plotted versus the Reynolds number in figure 10b. As already seen in the 2D plots it is visible that for the front position of the shock generator, the results at $Re_{\mathrm{u},\infty} = 12 \cdot 10^6 \frac{1}{\mathrm{m}}$ and $6 \cdot 10^6 \frac{1}{\mathrm{m}}$ are similar and $3 \cdot 10^6 \frac{1}{\mathrm{m}}$ quite different. At the back position the results of $Re_{\mathrm{u},\infty} = 6 \cdot 10^6 \frac{1}{\mathrm{m}}$ and $3 \cdot 10^6 \frac{1}{\mathrm{m}}$ are similar and $12 \cdot 10^6 \frac{1}{\mathrm{m}}$ is quite different. Considering figure 9a and the marked shock impingement positions an explanation would be that the shock impingement for $x_{\mathrm{shock}} = 239\,\mathrm{mm}$ is at the transition onset or inside the transition region for the higher Reynolds numbers and triggers a full transition. It is far upstream the transition region at the lowest Reynolds number. The SWBLI is not sufficent to trigger a transition to a fully turbulent boundary layer. In contrast to that the shock impingement for $x_{\mathrm{shock}} = 331\,\mathrm{mm}$ is at the transition onset or inside the transition region for the lower Reynolds numbers and triggers a full transition. But it is after the transition region of the highest Reynolds number and therefore there is no overshoot in the heat flux distribution. For the back position the shock from the leading edge reflected by the shock generator leads to a second peak in the Stanton number distributions of the higher Reynolds number cases. The effect described by Schülein and Wagner [7] of a small decrease in the Stanton number prior to the steep increase occurs only for $Re_{\mathrm{u},\infty} = 3 \cdot 10^6 \frac{1}{\mathrm{m}}$. For the higher Reynolds numbers there is also the a priori increase of the Stanton number.

Another interesting effect is the drop of the Stanton number after the shock impingement below the values of the free transition. This can be observed in figure 10a for $x_{\mathrm{shock}} = 239\,\mathrm{mm}$ and $Re_{\mathrm{u},\infty} = 12 \cdot 10^6 \frac{1}{\mathrm{m}}$ as well as $Re_{\mathrm{u},\infty} = 6 \cdot 10^6 \frac{1}{\mathrm{m}}$. Figure 10b reveals that the values drop even below the theoretical values of a turbulent boundary layer. Figures 8d and 8f shows an interference coming from the sides at the end of the insert. Therefore a possible explanation are the expansion waves emerging from the trailing edge of the shock generator.

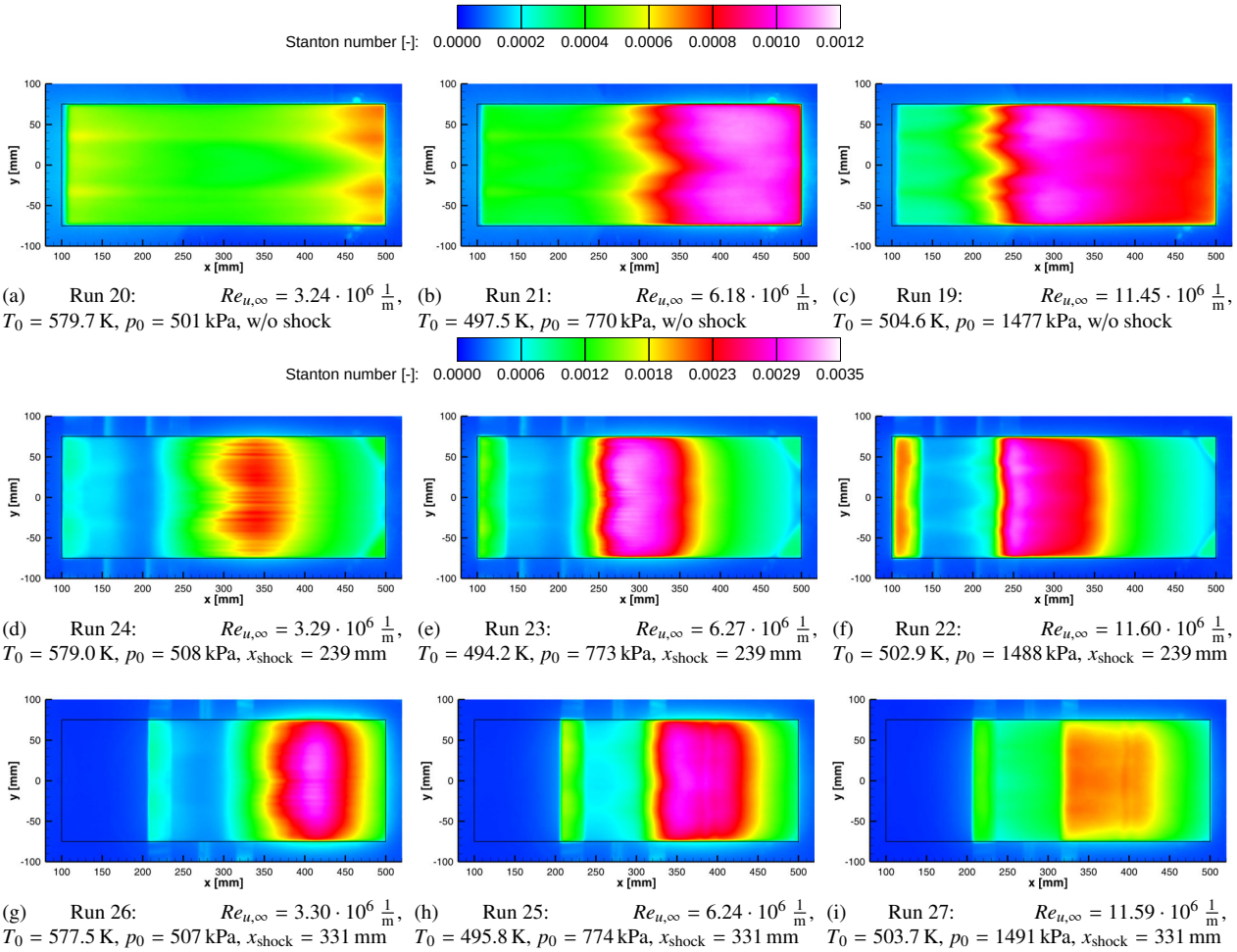

(a) Run 20: $Re_{u,\infty} = 3.24 \cdot 10^6 \frac{1}{\mathrm{m}}$, $T_0 = 579.7\,\mathrm{K}$, $p_0 = 501\,\mathrm{kPa}$, w/o shock

(b) Run 21: $Re_{u,\infty} = 6.18 \cdot 10^6 \frac{1}{\mathrm{m}}$, $T_0 = 497.5\,\mathrm{K}$, $p_0 = 770\,\mathrm{kPa}$, w/o shock

(c) Run 19: $Re_{u,\infty} = 11.45 \cdot 10^6 \frac{1}{\mathrm{m}}$, $T_0 = 504.6\,\mathrm{K}$, $p_0 = 1477\,\mathrm{kPa}$, w/o shock

(d) Run 24: $Re_{u,\infty} = 3.29 \cdot 10^6 \frac{1}{\mathrm{m}}$, $T_0 = 579.0\,\mathrm{K}$, $p_0 = 508\,\mathrm{kPa}$, $x_{\mathrm{shock}} = 239\,\mathrm{mm}$

(e) Run 23: $Re_{u,\infty} = 6.27 \cdot 10^6 \frac{1}{\mathrm{m}}$, $T_0 = 494.2\,\mathrm{K}$, $p_0 = 773\,\mathrm{kPa}$, $x_{\mathrm{shock}} = 239\,\mathrm{mm}$

(f) Run 22: $Re_{u,\infty} = 11.60 \cdot 10^6 \frac{1}{\mathrm{m}}$, $T_0 = 502.9\,\mathrm{K}$, $p_0 = 1488\,\mathrm{kPa}$, $x_{\mathrm{shock}} = 239\,\mathrm{mm}$

(g) Run 26: $Re_{u,\infty} = 3.30 \cdot 10^6 \frac{1}{\mathrm{m}}$, $T_0 = 577.5\,\mathrm{K}$, $p_0 = 507\,\mathrm{kPa}$, $x_{\mathrm{shock}} = 331\,\mathrm{mm}$

(h) Run 25: $Re_{u,\infty} = 6.24 \cdot 10^6 \frac{1}{\mathrm{m}}$, $T_0 = 495.8\,\mathrm{K}$, $p_0 = 774\,\mathrm{kPa}$, $x_{\mathrm{shock}} = 331\,\mathrm{mm}$

(i) Run 27: $Re_{u,\infty} = 11.59 \cdot 10^6 \frac{1}{\mathrm{m}}$, $T_0 = 503.7\,\mathrm{K}$, $p_0 = 1491\,\mathrm{kPa}$, $x_{\mathrm{shock}} = 331\,\mathrm{mm}$

Figure 8: Distribution of the Stanton number on the PEEK insert (rectangle) for high and low unit Reynolds number and various shock positions

4.3 Kulite sensors

The quality of the measurements with Kulite sensors is limited due to the fact that their measuring range was chosen for HEG. In addition the measured values drift probably due to the temperature increase. Therefore the averaged values of one second shortly after the tunnel start are used for figure 11a. The measured values p_{Kulites} are normalized with the static pressure of the free stream p_∞. The pressure increase and decrease after the SWBLI is independent of the unit Reynolds number. In contrast to that the pressure increase before the SWBLI caused by the separation shock depends on the unit Reynolds number and reveals the increasing size of the separation bubble with a decreasing unit Reynolds number. The shift of the SWBLI downstream increases the maximum pressure increase during the interaction.

4.4 PCB and ALTP gauges

Although it was “pushing the envelope” of the sensors design, PCB sensors have been successfully used to measure the second Mack mode in H2K before. In contrast to that it was the first time that an ALTP sensor was used in H2K.

The frequency spectra of the PCB and ALTP sensors shown in the figure 11 are averaged over five seconds during the steady flow phase. Figures 11b to 11d shows that within a free transition process the second Mack mode is measurable for all Reynolds numbers. It also demonstrates that the ALTP sensor and PCB 2, which have the same X-coordinate, have also similar frequency spectra. There is some noise in the unfiltered PCB spectra around 30 and 60 and above 200 kHz. The noise level of the ALTP sensor is much lower, but it shows the same interferences at 60 kHz. Nevertheless the peak of the second Mack mode is clearly detectable. Its frequency depends on the path length and the unit Reynolds number and is between 70 and 200 kHz. Consistent with the results of the IMENS-3C project on a transition cone the frequency at the same path length increases with an increasing unit Reynolds number and decreases

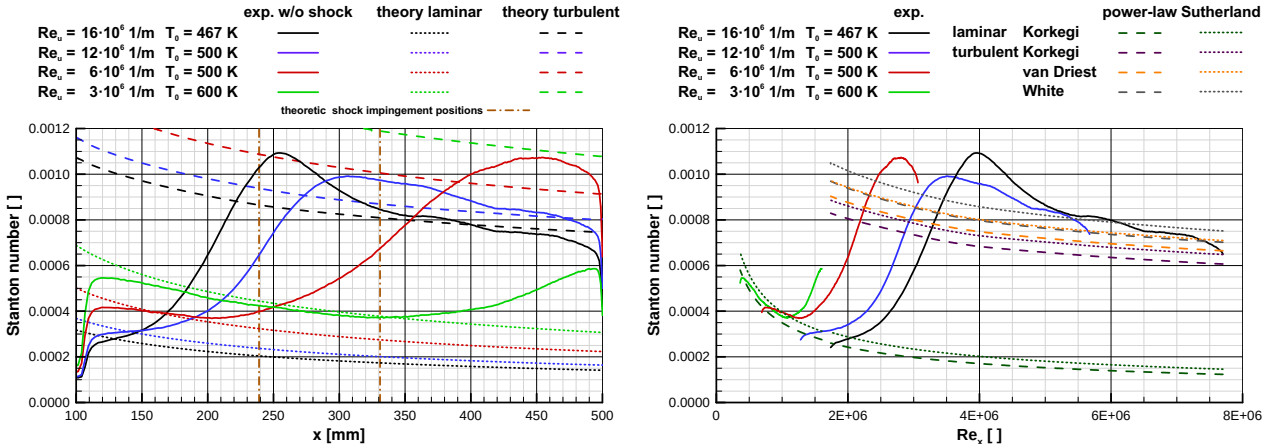

(a) Stanton number vs. path length

(b) Stanton number vs. Reynolds number

Figure 9: Measured Stanton number of free transition compared to theoretic curves for various Reynolds numbers in the symmetry plane

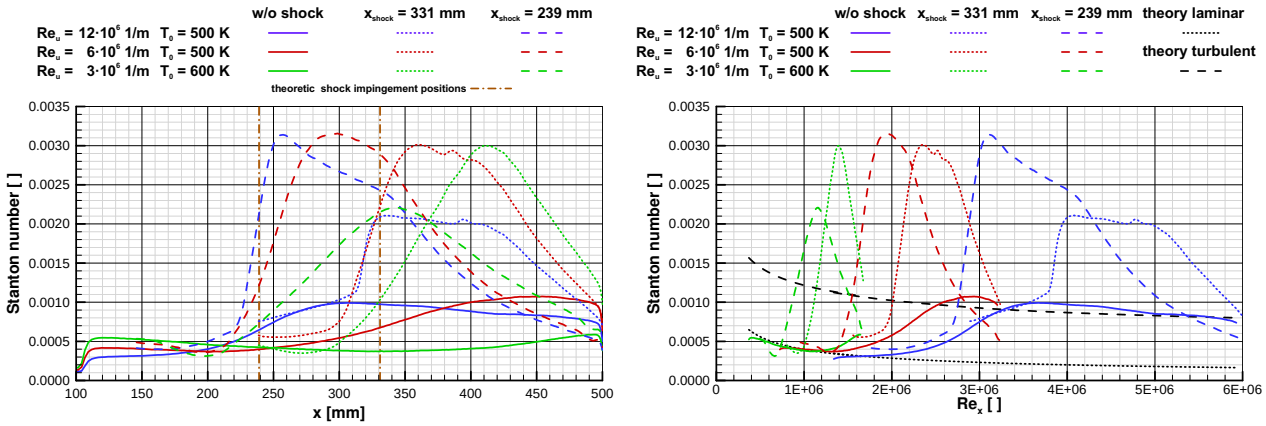

(a) Stanton number vs. path length

(b) Stanton number vs. Reynolds number

Figure 10: Measured Stanton number for various Reynolds numbers and various shock impingement positions in the symmetry plane

with an increasing path length for the same unit Reynolds number [11]. The amplification of the amplitude in the transition region and the destruction of the second Mack mode towards the end of the transition can also be confirmed. Due to the increasing length of the free transition region with a decreasing unit Reynolds number (figure 9a), the second Mack mode is detected by just one PCB in the high, by two PCBs in the middle and three PCB sensors in the low unit Reynolds number runs. As the ALTP has a lower noise ratio the development of the second Mack mode is in fact also detected at a fourth X-position for $Re_{\mathrm{u},\infty} = 3 \cdot 10^6 \, \frac{1}{\mathrm{m}}$.

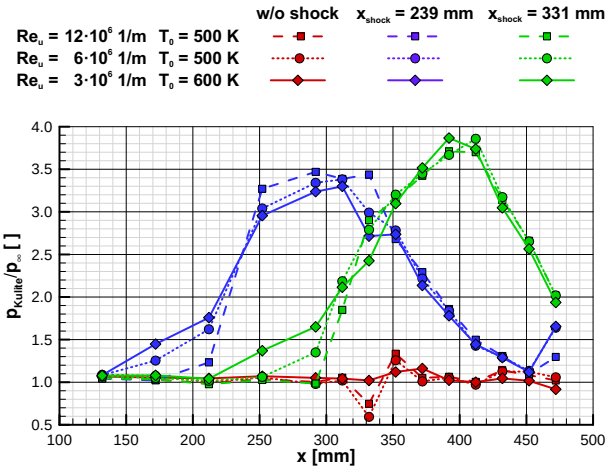

(a) Kulite measurements p_{Kulites} after 1.0 s normalized with the static pressure of the free stream p_∞

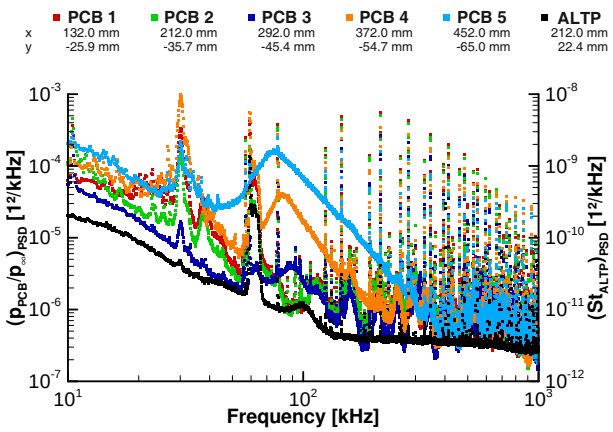

(b) Run 32: $Re_{u,\infty} = 3.30 \cdot 10^6 \frac{1}{\text{m}}$, $T_0 = 576.9\,\text{K}$, $p_0 = 506\,\text{kPa}$, w/o shock

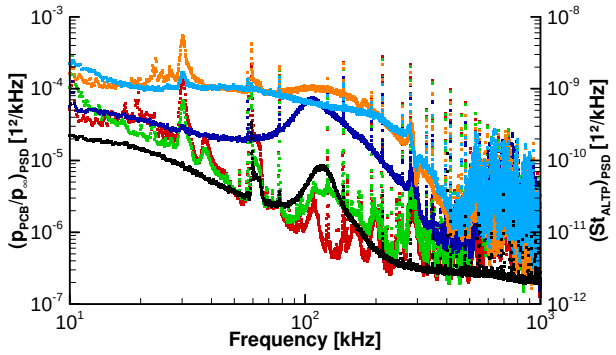

(c) Run 31: $Re_{u,\infty} = 6.17 \cdot 10^6 \frac{1}{\text{m}}$, $T_0 = 497.7\,\text{K}$, $p_0 = 768\,\text{kPa}$, w/o shock

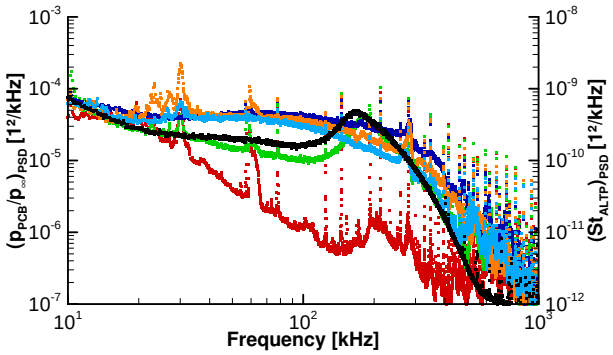

(d) Run 30: $Re_{u,\infty} = 11.65 \cdot 10^6 \frac{1}{\text{m}}$, $T_0 = 503.5\,\text{K}$, $p_0 = 1498\,\text{kPa}$, w/o shock

Figure 11: Averaged values of the static Kulite measurements and averaged frequency spectra of the PCB and ALTP sensors

5. Conclusion

An experimental study on laminar to turbulent transition has been carried out in the hypersonic wind tunnel H2K. For the tests a model, which had three inserts with different instrumentation set-up, has been used. For the study of shock induced transition a shock generator was placed at two different positions above the base plate. The same model was used in the Shock Tunnel HEG before testing in H2K. In order to achieve free transition in H2K a new sharp leading edge was necessary.

The transition region could be visualized by means of the infrared thermography and using a PEEK insert with low thermal conductivity. Additional flow visualization was carried out by Schlieren pictures. Kulite and PCB sensors measured static and dynamic pressure distribution along the base plate. For the first time thin film gauges, coaxial thermocouples and ALTP sensors were used for the heat flux measurements. It has been noticed that the poor signal to noise ratio of the thin film gauges and the coaxial thermocouples does not allow to measure the dynamics of the heat flux. In contrary ALTP sensor provided useful static and dynamic data. The Schlieren photography shows the position of the shock wave at the leading edge and the expansion waves at the trailing edge of the shock generator. When the shock generator is at the back position, the reflection of the nose shock on the shock generator and its impingement on the base plate are also visible. An increasing size of the separation bubble at the SWBLI with a decreasing Reynolds number could be quantified with the help of the Schlieren photographs as well as the pressure measurements with Kulite sensors.

The known influence of the Reynolds number on the boundary layer transition as well as the effect of the shock wave boundary layer interaction (SWBLI) onto the transition process could be verified. Depending on the position of the SWBLI compared to the free transition location, it is either an impingement into a fully developed turbulent boundary layer or the SWBLI triggers the transition process. If the shock impingement is close to the start of the free transition, the boundary layer becomes fully turbulent afterwards. If the shock impingement is far upstream the free

transition, the boundary becomes transitional, but relaminarizes afterwards. Second (Mack) modes could be measured with the PCB sensors as well as the ALTP sensor.

Acknowledgements

This work has been funded by the ESA TRP "Laminar to Turbulent Transition in Hypersonic Flows". The contributions of the other project partners and of the study manager Johan Steelant is gratefully acknowledged. Also the great effort and support of the H2K operation team is gratefully acknowledged.

References

[1] Ames, R. S. 1953. Equations, Tables, and Charts for Compressible Flow. Technical Report 1135, National Advisory Committee for Aeronautics, Moffett Field, California.

[2] Henckels, A. and Gruhn, P. 2004. Study on Aerothermal Effects of Viscous Shock Interaction in Hypersonic Inlets. In *Proceedings of the Fifth European Symposium on Aerothermodynamics for Space Vehicles*, pages 553–558, Cologne. European Space Agency.

[3] Hopkins, E. J. and Inouye, M. 1971. An Evaluation of Theories for Predicting Turbulent Skin Friction and Heat Transfer on Flat Plates at Supersonic and Hypersonic Mach Numbers. *AIAA Journal*, 9(6).

[4] Korkegi, R. H. 1962. Hypersonic Aerodynamics. Technical Report Course Note 9, von Karman Institute, Rhode-Saint-Genese.

[5] Müller, L. and Henckels, A. 1997. Visualization of High Speed Boundary Layer Transition with FPA Infrared Technique. In *Notes on Numerical Fluid Mechanics*, volume 60, pages 245–252.

[6] Niezgodka, F.-J. 2001. *Der Hyperschallwindkanal H2K des DLR in Köln-Porz (Stand 2000).* DLR-Mitteilungen. Deutsches Zentrum für Luft- und Raumfahrt e. V., Köln.

[7] Schülein, E. and Wagner, A. 2012. Ludwieg-Tube Experiments on the Effects of Laminar-Turbulent Transition on the SWBLI at Mach 6, ESA-TRP "Laminar to Turbulent Transition in Hypersonic Flows" TN 4110. Technical Report DLR-IB 224-2011 A 64, German Aerospace Center, Göttingen.

[8] Tsai, R. Y. 1987. A Versatile Camera Calibration Technique for High-Accuracy 3D Machine Vision Metrology Using Off-the-Shelf TV Cameras and Lenses. *Journal of Robotics and Automation*, RA-3(4).

[9] van Driest, E. R. 1956. The problem of aerodynamic heating. *Aeronautical Engineering Review*.

[10] White, F. M. 2006. *Viscous fluid flow*. McGraw-Hill, New York, 3rd edition.

[11] Willems, S. and Gülhan, A. 2012. Damping of the Second Mode Instability with Regular and Random Porous Surfaces on a Slender Cone in Hypersonic Flow. In *AVT-200 Specialists' Meeting on Hypersonic Laminar-Turbulent Transition*, San Diego, California. NATO RTO.